

1 SDUST2020MGCR: a global marine gravity change rate model
2 determined from multi-satellite altimeter data

3 Fengshun Zhu ^{1,2,3}, Jinyun Guo ¹, Huiying Zhang ¹, Lingyong Huang ⁴, Heping Sun ^{2,3},
4 Xin Liu ¹

5 1 College of Geodesy and Geomatics, Shandong University of Science and
6 Technology, Qingdao 266590, China

7 2 State Key Laboratory of Geodesy and Earth's Dynamics, Innovation Academy for
8 Precision Measurement Science and Technology, Chinese Academy of Sciences,
9 Wuhan 430077, China

10 3 University of Chinese Academy of Sciences, Beijing 100049, China

11 4 State Key Laboratory of Geo-Information Engineering, Xian 710054, China

12
13 Corresponding Author: Jinyun Guo, Email: jinyunguo1@126.com

14
15 Abstract. Investigating global time-varying gravity field mainly depends on
16 GRACE/GRACE-FO gravity data. However, satellite gravity data exhibits low spatial
17 resolution and signal distortion. ~~The satellite altimetry is an important technique for~~
18 ~~observing global ocean, providing continuous multi-year data that enables the study of~~
19 ~~high-resolution time-varying marine gravity.~~ Satellite altimetry is an important
20 technique for observing global ocean and provides many consecutive years data,
21 which enables the study of high-resolution marine gravity variations. This study aims
22 to construct a high-resolution marine gravity change rate (MGCR) model using multi-
23 satellite altimetry data. Initially, multi-satellite altimetry data and ocean temperature-
24 salinity data from 1993 to 2019 are utilized to estimate the altimetry sea level change
25 rate (SLCR) and steric SLCR, respectively. Subsequently, the mass-term SLCR is
26 calculated. Finally, based on mass-term SLCR, ~~we construct~~ the global MGCR model
27 on 5'×5' grids (SDUST2020MGCR) is constructed by applying the spherical
28 harmonic function method and mass load theory. Comparisons and analyses are
29 conducted between SDUST2020MGCR and GRACE2020MGCR resolved from
30 GRACE/GRACE-FO gravity data. The spatial distribution characteristics of
31 SDUST2020MGCR and GRACE2020MGCR are similar in the sea areas where
32 gravity changes significantly, such as ~~the seas near some ocean currents~~ the eastern
33 seas of Japan, the western seas of the Nicobar Islands, and the southern seas of

34 Greenland. The statistical mean values of SDUST2020MGCR and
35 GRACE2020MGCR in global and local oceans are all positive, indicating that MGCR
36 is rising. Nonetheless, differences in spatial distribution and statistical results exist
37 between SDUST2020MGCR and GRACE2020MGCR, primarily attributable to
38 spatial resolution disparities among altimetry data, ocean temperature-salinity data,
39 and GRACE/GRACE-FO data. Compared with GRACE2020MGCR,
40 SDUST2020MGCR has higher spatial resolution and excludes stripe noise and
41 leakage errors. The high-resolution MGCR model constructed using altimetry data
42 can reflect the long-term marine gravity change in more detail, which is helpful ~~to~~
43 study in studying Earth mass migration seawater mass migration and its associated
44 geophysical processes. The SDUST2020MGCR model data is available at
45 <https://zenodo.org/records/10098524> <https://zenodo.org/records/10701641> (Zhu et al.,
46 2024).

47 **1 Introduction**

48 The Earth's large-scale mass migration ~~will~~ can cause spatiotemporal changes of
49 the Earth's gravity field (Li et al., 2021). The ocean accounts for about 71% of the
50 global area, and the determination of time-varying marine gravity field is an important
51 research content of the Earth's time-varying gravity field. The high-precision and
52 high-resolution spatiotemporal change information of marine gravity field is useful
53 for monitoring related geophysical processes such as ~~the~~ ice melting, ocean dynamic
54 processes and crustal deformation.

55 Investigating the Earth's time-varying gravity field mainly relies on repeated
56 observations ~~data~~ of ground gravity and satellite gravity. The large-scale regional
57 gravity field changes can be studied utilizing the multi-year gravity measurement data
58 on the relative gravity surveying network (Liang et al., 2016). The precise gravity
59 field changes in small areas can be investigated using repeated measurement data
60 from absolute gravimeters on gravity stations (Greco et al., 2012). However, the
61 gravimeter observation is costly, and gravimeter marine observation requires a lot of
62 manpower, material and financial resources. The satellite gravity provides the
63 possibility for repeated observations of the Earth's large-scale gravity field. At present,
64 the high-low satellite-to-satellite tracking, low-low satellite-to-satellite tracking and
65 satellite gravity gradient measurement technologies have been developed. The
66 successfully launched gravity satellites include CHAMP, GRACE/GRACE-FO and

67 GOCE (Flechtner et al., 2021). Among them, the GRACE/GRACE-FO gravity
68 satellite data is the most widely ~~used~~ utilized. The GRACE/GRACE-FO ~~uses the~~
69 adopts the gravity measurement technology of low-low satellite-to-satellite tracking
70 model; ~~it~~ The GRACE/GRACE-FO can obtain time-varying gravity with an accuracy
71 of about 0.1 mGal (Flury and Rummel, 2005) and time-varying equivalent water
72 height with an accuracy of approximately 1 cm (Wahr et al., 2004), but its spatial
73 resolution of one-half wavelength is only 400-500 km (Tapley et al., 2004), the
74 resolution is low, and there is large signal distortion and leakage errors.

75 The satellite altimetry technique can quickly and repeatedly obtain high-
76 precision global ocean information, becoming an important means to observe and
77 study the ocean. Products such as mean sea level model, static marine gravity field
78 model, and sea level change dataset can be extracted or derived by using altimetry sea
79 surface height (SSH). The Technical University of Denmark team ~~focuses~~ focused on
80 model improvement in the Arctic Ocean, utilizing multi-satellite altimetry data to
81 construct the global mean sea level model (Andersen et al., 2021, 2023) and the
82 global marine gravity field model (Andersen and Knudsen, 2020). The Shandong
83 University of Science and Technology (SDUST) team also ~~constructs~~ constructed the
84 global mean sea level model (Yuan et al., 2023) and the marine gravity field model
85 (Zhu et al., 2022) using altimetry data, ~~improving the model accuracy in offshore~~
86 areas and the accuracy of the model was improved in the offshore region. The
87 European Copernicus Marine Environment Monitoring Service ~~uses~~ used altimetry
88 data to produce and release daily and monthly gridded sea level change dataset
89 products (Taburet et al., 2019). The Scripps Institution of Oceanography in the United
90 States also ~~develops~~ developed the global altimetry marine gravity field model
91 (Sandwell et al., 2021). So far, the altimetry SSH ~~is of~~ has been at the centimeter-
92 level accuracy, and the calculated global sea level changes have reached millimeter-
93 level accuracy (Nerem et al., 2010). The global altimetry marine gravity field model
94 has had a spatial resolution better than 10 km, and the calculation accuracy ~~is~~ has been
95 about 1 mGal (Sandwell et al., 2013). However, few studies have applied altimetry
96 means to time-varying marine gravity. This paper aims to utilize multi-satellite
97 altimetry data to construct a global marine gravity change rate (MGCR) model
98 (SDUST2020MGCR).

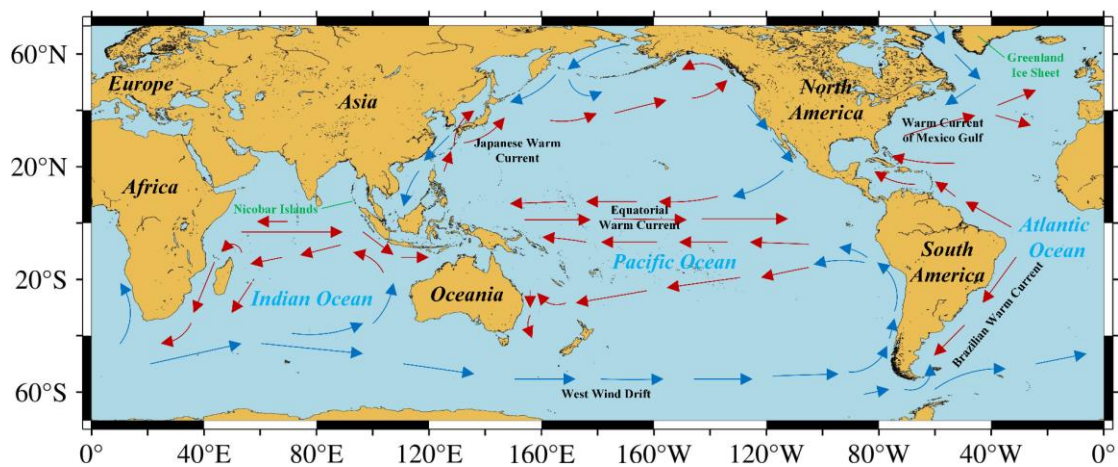
99 The seawater migration causes changes of the Earth's shape and gravity field. In
100 this study, we propose to utilize the sea level change rate (SLCR) to calculate the

101 MGCR. Firstly, multi-satellite altimetry data from 1993 to 2019 are utilized to
 102 estimate the long-term altimetry SLCR, and EN4.2.1 ocean temperature and salinity
 103 data from 1993 to 2019 are utilized to estimate the long-term steric SLCR. Then, the
 104 steric SLCR is subtracted from altimetry SLCR to calculate the mass-term SLCR.
 105 Finally, this paper applies the method proposed by ~~Zhu et al.~~ (Zhu et al., (2023) to
 106 estimate long-term MGCR, that is utilizing the mass-term SLCR to construct a global
 107 MGCR model based on mass load theory and spherical harmonic function method. In
 108 Sect. 2, the study area and data sources are introduced. In Sect. 3, the methods of
 109 altimetry SLCR estimation, steric SLCR estimation, mass-term SLCR estimation and
 110 MGCR estimation are described in detail, respectively. In Sect. 4, the global SLCR
 111 and MGCR models are given, and the model comparisons and analyses are performed.
 112 In Sect. 5, the conclusion is presented.

113 2 Study area and data

114 2.1 Study area

115 ~~This paper selects the ocean covering 0-360°E and 70°S-70°N as the study area,~~
 116 In this paper, the ocean covering 0-360°E and 70°S-70°N is selected as the study area,
 117 as shown in Fig. 1. There are various mass migration phenomena on Earth, such as
 118 ocean currents that move seawater in a certain direction, the subduction of oceanic
 119 plates to continental plates that form island arcs (e.g. Nicobar Islands) and trenches,
 120 and the melting ice due to global warming that reduce the mass of Greenland and
 121 Antarctic. The mass migration causes changes in the Earth's gravity field.
 122 Constructing the high-resolution time-varying marine gravity model is helpful for the
 123 study of the material migration movement.



124
 125 Figure 1. The study area ~~covering~~ covers 0-360°E and 70°S-70°N. The base map was created
 126 using Generic Mapping Tools, then we have roughly marked the Continents, the Oceans and the

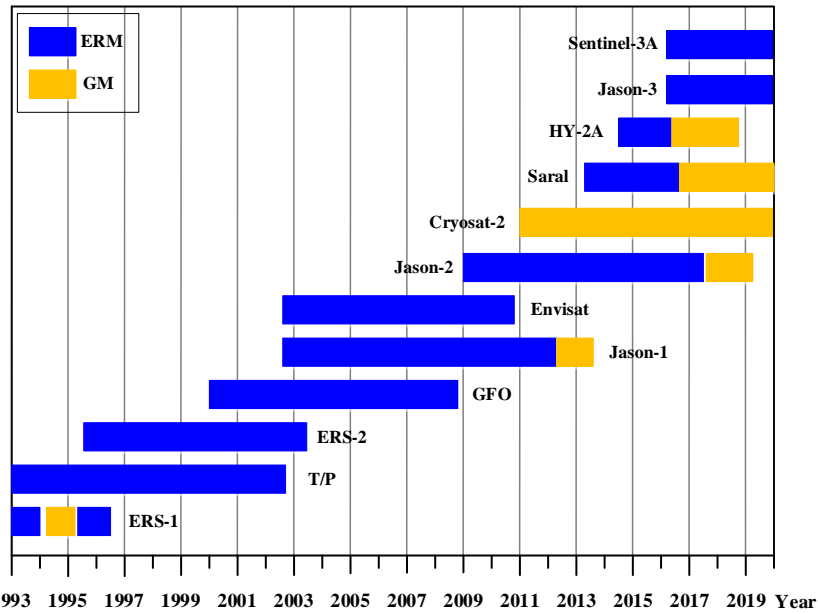
127 local sea areas with obvious gravity changes. Red arrows indicate areas where warm currents pass,
128 blue arrows indicate areas where cold currents pass, the Nicobar Islands and Greenland Ice Sheet
129 are also marked.

130 **2.2 L2P satellite altimetry data**

131 The satellite altimetry data includes products at different levels: Level-0 (L0),
132 Level-1 (L1), Level-2 (L2), Level-2 Plus (L2P) and Level-3 (L3). The L0 product is
133 raw telemetered data. The L0 product is corrected for instrumental effects to obtain
134 the L1 product. The L1 product is corrected for geophysical effects to obtain the L2
135 product. The geophysical effects corrections include corrections for dry and wet
136 tropospheric effects, ionospheric effects, ocean state bias, ocean tides, solid tides,
137 polar tides and atmospheric pressure. The L2 product is also called the geophysical
138 data records (GDR) product. Based on the L2 product, the correction model is
139 updated and replaced, and ~~the~~ new quality control is carried out, such as data
140 validation, data editing and algorithmic improvement, and finally, the L2P product is
141 ~~obtained-produced~~ (CNES, 2020). The L3 product is processed river and lake water
142 level time series data.

143 The L2P product is released by the AVISO (Archiving, Validation and
144 Interpretation of Satellite Oceanographic) data center (<https://www.aviso.altimetry.fr/>)
145 of the French Centre National d'Études Spatiales (CNES). The L2P product includes
146 data such as sea level anomaly, mean sea level, environmental parameters, and
147 geophysical correction models. Therefore, ~~the corresponding SSH can be calculated~~
148 ~~using L2P product as needed~~ the L2P product can be utilized to calculate the required
149 SSH. This study utilizes SSH data derived from L2P product to calculate multiple
150 mean sea level models, and construct sea level time series data, and finally, the least
151 squares model is applied to estimate high-resolution SDUST altimetry SLCR (Yuan et
152 al., 2021).

153 In this study, the L2P product from January 1993 to December 2019 is selected,
154 including two observation mission data of 12 altimetry satellites, as shown in Fig. 2.
155 The ERM (Exact Repeat Mission) data is observed by ERS-1/2, Topex/Poseidon (T/P),
156 Geosat Follow On (GFO), Envisat, Jason-1/2/3, HaiYang-2A (HY-2A), Saral, and
157 Sentinel-3A, and the GM (Geodetic Mission) data is observed by ERS-1, Jason-1/2,
158 HY-2A, Cryosat-2, and Saral.



159

160 Figure 2. The multi-satellite altimetry data is utilized in this study. The horizontal axis marks the
 161 observation time, and the vertical axis marks the name of the altimetry satellite. Blue represents
 162 ERM (Exact Repeat Mission) data, and orange represents GM (Geodetic Mission) data.

163 **2.3 EN4 ocean temperature and salinity data**

164 The ocean temperature and salinity data is important basic data for studying
 165 global climate change and ocean change. This data can be used to study ~~seawater~~
 166 ~~volume change~~ocean volume changes caused by changes in seawater temperature and
 167 salinity, and further to predict global climate disasters. The Argo (Array for Real-Time
 168 Geostrophic Oceanography) project aims to use Argo floats to form a global ocean
 169 observation network to measure the depth, temperature, salinity and other ~~data~~
 170 ~~parameters~~ of the ocean in real time (Riser et al., 2016). Now, nearly 4000 Argo floats
 171 are in working condition, which provides basic data for constructing global ocean
 172 temperature and salinity data products.

173 The various ocean temperature and salinity data products are all affected by
 174 irregular floats distribution and model gridding, and their accuracy is basically the
 175 same (Hosoda et al., 2008; Roemmich and Gilson, 2009). This study utilizes the
 176 EN4.2.1 monthly ocean temperature and salinity product from January 1993 to
 177 December 2019 released by the Met Office ([https://argo.ucsd.edu/data/argo-data-
 178 products/](https://argo.ucsd.edu/data/argo-data-products/)) to study the ~~seawater volume change~~ocean volume change and calculate
 179 the steric SLCR. The grid size of EN4.2.1 data is 1°×1° (Good et al., 2013).

180 **2.4 AVISO monthly sea level anomaly data**

181 The AVISO data center of the CNES also released monthly sea level anomaly

182 data product on 15'×15' grids. The sea level anomaly is referenced to the mean sea
 183 level from 1993 to 2012. This product can resolve-discern sea level changes on a scale
 184 of 150-200 km, with an accuracy of centimeter-level in most sea areas worldwide
 185 around-the-world (Ducet et al., 2000). The AVISO monthly sea level anomaly data
 186 integrates observation data from Jason-1/2/3, T/P, Envisat, ERS-1/2, Geosat and GFO,
 187 and has been corrected for geophysical influences, such as dry and wet tropospheric
 188 influence, ionospheric delay, tides, and the dynamic atmosphere. This study utilizes
 189 AVISO monthly sea level anomaly grid data from January 1993 to December 2019 to
 190 estimate AVISO altimetry SLCR.

191 2.5 ICE-6G glacial isostatic adjustment model

192 The glacial isostatic adjustment (GIA) is the response of the viscoelastic earth to
 193 changes in surface ice and seawater load during the last glacial period. The marine
 194 gravity changes resolved from satellite gravity data and satellite altimetry data include
 195 not only the impact of contemporary Earth mass migration, but also the impact of
 196 solid earth mass redistribution driven by GIA. In the research on various Earth science
 197 issues, the GIA effect is usually deducted as a linear term. Argus and Peltier et al.
 198 (Argus et al., 2014; Peltier et al., 2015) provided the ICE-6G fully normalized
 199 geopotential trend coefficients \dot{C}_{lm}^{GIA} and \dot{S}_{lm}^{GIA} , with the degree and order fully
 200 expanded to 256. In this study, the degree of GIA model is truncated to the 60, which
 201 will be deducted from GRACE and altimetry observations. The spherical harmonic
 202 coefficients in the ICE-6G model correspond to the interannual trend, and we need to
 203 calculate the GIA coefficients for each month to deduct the GIA effect from the
 204 GRACE monthly harmonic coefficients. Based on the ICE-6G fully normalized
 205 geopotential annual trend coefficients \dot{C}_{lm}^{GIA} and \dot{S}_{lm}^{GIA} , the GIA corrected geopotential
 206 coefficients ΔC_{lm}^{GIA} and ΔS_{lm}^{GIA} for each month from January 1993 to December 2019
 207 can also be calculated:

$$208 \begin{cases} \Delta \bar{C}_{lm}^{GIA}(N) = (N/12) \times \dot{C}_{lm}^{GIA} & (N = 1, 2, \dots, 324) \\ \Delta \bar{S}_{lm}^{GIA}(N) = (N/12) \times \dot{S}_{lm}^{GIA} & (N = 1, 2, \dots, 324) \end{cases} \quad (1)$$

209 Where N represents the month, and there are 324 months from January 1993 to
 210 December 2019. The GIA corrected geopotential annual trend coefficients and GIA
 211 corrected geopotential coefficients are utilized to correct the altimetry MGCRCR and
 212 GRACE/GRACE-FO monthly gravity data, respectively, which can deduct the marine

213 gravity changes due to the long-term oceanic crust deformation driven by GIA.

214 **2.6 GRACE/GRACE-FO monthly geopotential spherical harmonics data**

215 The main purpose of the GRACE system and the GRACE-FO system is to obtain
216 the long-medium wavelength signals of the Earth's gravity field and to detect gravity
217 changes (Han et al., 2004). The orbit parameters of GRACE satellite and GRACE-FO
218 satellite are basically the same, with an orbit inclination of 89.5° and an orbit altitude
219 of about 500 km (Wouters et al., 2014). The main instruments carried by the satellites
220 are GPS receivers and ranging systems. The GRACE/GRACE-FO time-varying
221 gravity data mainly consists of Level-1, Level-2 and Level-3. ~~The Level-1 data is~~
222 ~~satellite orbit data~~ The Level-1 data is raw observations that include distance changes
223 between the dual-satellite, and acceleration changes due to the Earth's gravitational
224 variations. The Level-2 data is ~~Earth-global~~ time-varying gravity field model
225 expressed in spherical harmonic coefficient, which has been corrected for the effects
226 of ocean tides, solid tides, atmosphere tides, pole tides, and non-tidal variability in the
227 atmosphere and ocean (UTCSR, 2018). The Level-3 data is grid format data
228 represented by Mascon products.

229 The Center for Space Research at the University of Texas (UTCSR) released
230 GRACE/GRACE-FO Level-2 RL06 monthly geopotential spherical harmonics data,
231 including GSM and GAD data. The CSR_GSM data represents the estimation of
232 Earth's monthly average gravity field, and the degree and order ~~is-are~~ fully calculated
233 to 60. The CSR_GAD data represents the impact of non-tidal oceanic and
234 atmospheric pressure ~~to-on~~ the ocean bottom pressure. The International Center for
235 Global Earth Model (ICGEM, <http://icgem.gfz-potsdam.de/home>) provides
236 CSR_GSM data filtered by DDK2. The DDK2 is a non-isotropic filtering method, and
237 CSR_GSM_DDK2 contains less stripe noise.

238 The GRACE/GRACE-FO dataset has 180-months data between April 2002 and
239 December 2019, and any missing GRACE/GRACE-FO data are not reconstructed in
240 this study. The degree-1 coefficients supplementation, degree-2 and degree-3
241 coefficients replacement are performed on CSR_GSM_DDK2 data. In addition, to
242 match with the satellite altimetry data, the spherical harmonic coefficient of
243 CSR_GSM_DDK2 and CSR_GAD are linearly summed ~~in a linear manner~~:

$$244 \begin{cases} \bar{C}_{lm}^{GRACE}(N) = \bar{C}_{lm}^{GSM}(N) + \bar{C}_{lm}^{GAD}(N) \\ \bar{S}_{lm}^{GRACE}(N) = \bar{S}_{lm}^{GSM}(N) + \bar{S}_{lm}^{GAD}(N) \end{cases} \quad (2)$$

Utilizing the mean spherical harmonic coefficient of 180-months gravity data as the reference gravity field. The mean spherical harmonic coefficient of 180-months gravity data is utilized as the reference gravity field, and the GRACE/GRACE-FO geopotential spherical harmonic coefficient variations $\Delta\bar{C}_{lm}^{GRACE}$ and $\Delta\bar{S}_{lm}^{GRACE}$ are calculated. Then the monthly equivalent seawater height (ESH) change is ~~obtained~~ calculated (Wahr et al., 1998; Godah, 2019):

$$\Delta ESH(N, \lambda, \theta) = \frac{a\rho_E}{3\rho_S} \cdot \sum_{l=0}^{60} \sum_{m=0}^l [(2l+1)/(1+k_l)] \cdot \bar{P}_{lm}(\cos\theta) \cdot [\Delta\bar{C}_{lm}^{GRACE}(N) \cos m\lambda + \Delta\bar{S}_{lm}^{GRACE}(N) \sin m\lambda] \quad (3)$$

$$\Delta ESH(N, \lambda, \theta) = a\rho_E / 3\rho_S \cdot \sum_{l=0}^{60} \sum_{m=0}^l (2l+1)/(1+k_l) \cdot \bar{P}_{lm}(\cos\theta) \cdot [\Delta\bar{C}_{lm}^{GRACE}(N) \cos m\lambda + \Delta\bar{S}_{lm}^{GRACE}(N) \sin m\lambda] \quad (3)$$

Where λ and θ are the geocentric longitude and colatitude of the calculation point, a (= 6378136.3 m) is the Earth equatorial radius, ρ_E (= 5514 kg/m³) is the Earth average density, and ρ_S (= 1028 kg/m³) is the seawater average density, l and m are degree and order of spherical harmonic coefficient, \bar{P} is the fully normalized associated Legendre function, k is the load Love number.

In this study, the GIA corrected geopotential coefficient is subtracted from the GRACE/GRACE-FO geopotential spherical harmonic coefficient variations:

$$\begin{cases} \Delta\bar{C}_{lm}(N) = \Delta\bar{C}_{lm}^{GRACE}(N) - \Delta\bar{C}_{lm}^{GIA}(N) \\ \Delta\bar{S}_{lm}(N) = \Delta\bar{S}_{lm}^{GRACE}(N) - \Delta\bar{S}_{lm}^{GIA}(N) \end{cases} \quad (4)$$

Then the monthly gravity change is calculated (Godah, 2019):

$$\Delta g(N, r, \lambda, \theta) = \frac{GM}{r^2} \sum_{l=0}^{60} \sum_{m=0}^l (l-1) \cdot (a/r)^l \cdot \bar{P}_{lm}(\cos\theta) \cdot [\Delta\bar{C}_{lm}(N) \cos m\lambda + \Delta\bar{S}_{lm}(N) \sin m\lambda] \quad (5)$$

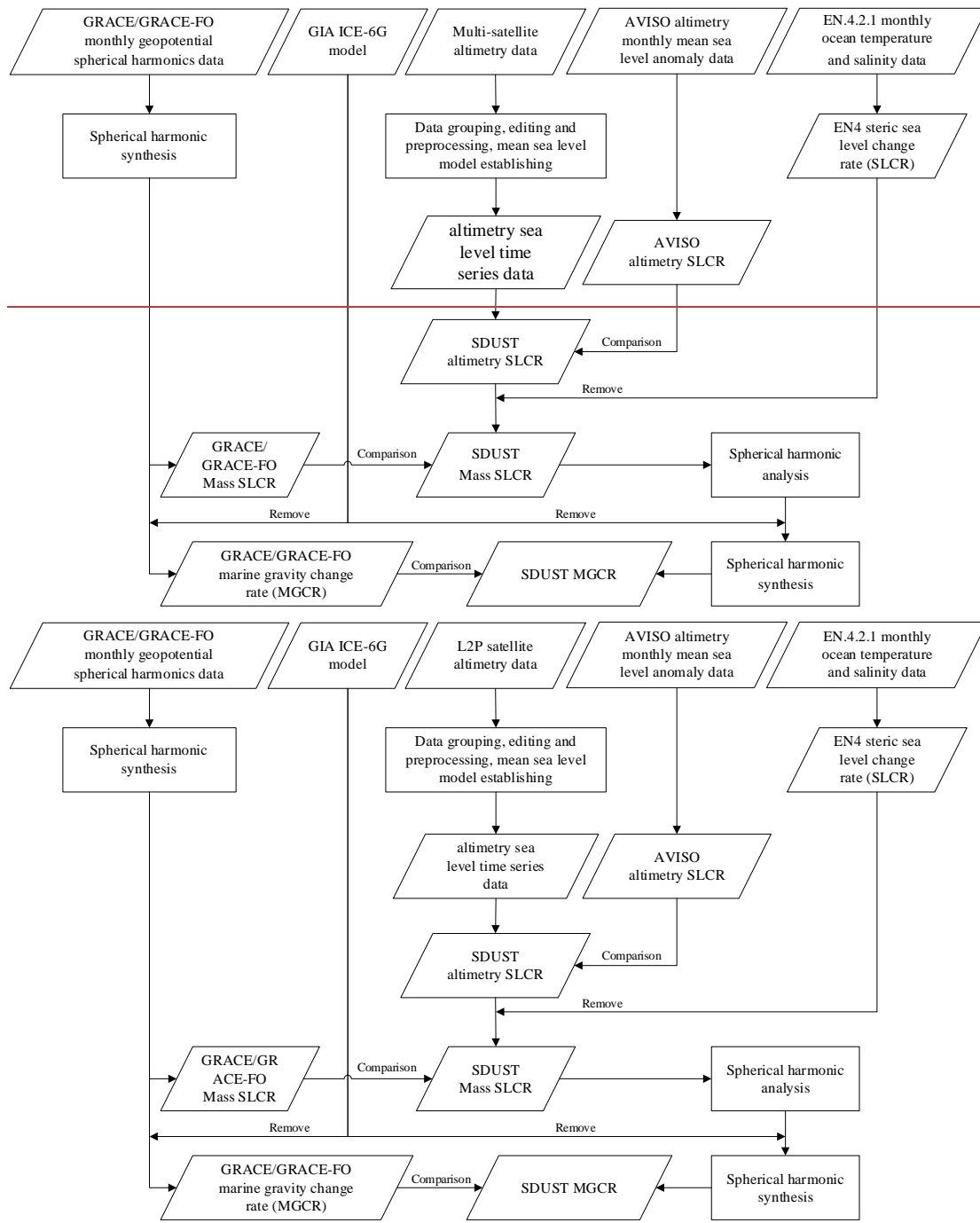
$$\Delta g(N, r, \lambda, \theta) = GM / r^2 \cdot \sum_{l=0}^{60} \sum_{m=0}^l (l-1) \cdot (a/r)^l \cdot \bar{P}_{lm}(\cos\theta) \cdot [\Delta\bar{C}_{lm}(N) \cos m\lambda + \Delta\bar{S}_{lm}(N) \sin m\lambda] \quad (5)$$

Where r is the geocentric radius, GM is the Earth's gravitational constant, and other variables are the same as before. This study applies the forward modelling method to correct signal leakage errors on GRACE/GRACE-FO ESH time series data and gravity time series data. Finally, the least squares model is applied to estimate the GRACE/GRACE-FO mass-term SLCR and MGCR, and the grid size is 1°×1°.

269 3 Methodology

270 The submarine plate motion, the melting of glaciers and ice sheets, and the
271 changes of ocean dynamics all lead to the spatial distribution changes of seawater
272 mass, which in turn causes changes of Earth's shape and gravity field. In static marine
273 gravity field studies, the geoid height is obtained by subtracting the mean sea surface
274 topography from the instantaneous altimetry SSH, and then the geoid height or geoid
275 gradient is utilized to construct the gravity field model (Gopalapillai and Mourad,
276 1979; Hwang et al., 2002). In this study of time-varying marine gravity based on
277 satellite altimetry, the mean sea surface topography is also regarded as invariable, and
278 it is proposed to utilize sea level change to study marine gravity change.

279 The flowchart of this research is shown in Fig. 3. Firstly, following the data
280 grouping, editing and preprocessing of L2P multi-satellite altimetry data, multiple
281 mean sea level models are calculated to construct altimetry sea level time series data,
282 and then the high-resolution SDUST altimetry SLCR is estimated by applying the
283 least squares model and is compared with the AVISO altimetry SLCR. Then the
284 SDUST mass-term SLCR is calculated by subtracting the EN4 steric SLCR from the
285 SDUST altimetry SLCR, and is compared with the GRACE/GRACE-FO mass-term
286 SLCR. Finally, based on the SDUST mass-term SLCR, the spherical harmonic
287 analysis, GIA effect deduction and spherical harmonic synthesis are performed to
288 obtain the SDUST MGCR, and the SDUST MGCR is compared with the
289 GRACE/GRACE-FO MGCR.



290

291

292 Figure 3. Flowchart of marine gravity change rate derivation from satellite altimetry data

293 **3.1 Estimation of altimetry SLCR**

294 **3.1.1 Data grouping and editing**

295 The multi-L2P satellite altimetry data from January 1993 to December 2019 are
 296 utilized to construct the high-precision and high-resolution altimetry SLCR model.
 297 The obliquity between the Moon orbit and the Earth equator is called the lunar
 298 declination angle, with a maximum value of 28.5° and a minimum value of 18.5° , and

299 its change cycle is 18.6 years. This study uses a 19-year moving window and a 1-year
300 moving step to divide the L2P products into 9 groups ([1993-2011](#), [1994-2012](#), [1995-](#)
301 [2013](#), [1996-2014](#), [1997-2015](#), [1998-2016](#), [1999-2017](#), [2000-2018](#), [2001-2019](#)) (Yuan
302 et al., 2020a), which can attenuate the ocean effect of a typical tide with 18.6 years. In
303 addition, in order to improve the modeling accuracy, the low-quality SSH data is
304 excluded according to the thresholds for altimeter, radiometer and geophysical
305 parameters defined in the L2P product handbook (CNES, 2020).

306 **3.1.2 Data preprocessing**

307 Each group of SSH data needs to perform the ocean variability correction to
308 attenuate SSH anomalous variation, SSH seasonal variation and radial orbit error. For
309 the ERM data, the collinear adjustment method is applied to perform ocean variability
310 correction (Rapp et al., 1994). The steps of this method are as follows: firstly, the
311 track with the most observation points among all collinear tracks is selected as the
312 reference track; then, the SSH of each point on other period collinear tracks is
313 interpolated to [the](#) corresponding point on the reference track; finally, the average
314 value of the SSH at each point is calculated to obtain a mean track.

315 The tracks of GM data are not collinear, so the GM data cannot [useapply](#) the
316 collinear adjustment to perform the ocean variability correction. In this study, the
317 ERM data of T/P series satellites (T/P, Jason-1/2/3) is continuous from 1993 to 2019,
318 thus the tracks of T/P series ERM data after collinear adjustment are selected as
319 reference tracks (Yuan et al., 2021). Then, the SSH difference of the T/P series ERM
320 data between the reference track point and the corresponding collinear track point is
321 calculated (Yuan et al., 2020b). Finally, the SSH correction on the GM track is
322 obtained using the space-time objective analysis interpolation (Yuan et al., 2020b;
323 Schaeffer et al., 2012), and the ocean variability correction for GM data of each
324 satellite is performed.

325 The short-wavelength ocean variability signals, radial orbit error residuals and
326 geophysical correction residuals in SSH data still affect the modeling of mean sea

327 level. This study uses the crossover adjustment based on the posterior compensation
 328 theory of error to continue the correction of SSH data. The details of this crossover
 329 adjustment method were described by ~~Huang et al and Yuan et al~~ (Huang et al., (2008);
 330 and Yuan et al., (2020b)). The steps of this method are as follows: firstly, the
 331 observation equation of altimetry satellite at the crossover point is established, and the
 332 conditional adjustment is performed to obtain the SSH correction v at the crossover
 333 point; then, for each altimetry track, a mixed polynomial error model $f(t)$ with
 334 independent variable of the measurement time t at observation point is established
 335 (Yuan et al., 2021):

$$336 \quad f(t) = a_0 + a_1(t - T_0) + \sum_{i=1}^M (b_i \cdot \cos(2\pi i \cdot (t - T_0) / (T_1 - T_0)) + c_i \cdot \sin(2\pi i \cdot (t - T_0) / (T_1 - T_0))) \quad (6)$$

337 Where a_0 , a_1 , b_i and c_i ($i = 1, 2, \dots, M$) are the parameters that need to be
 338 determined, the value of M can be determined based on the length of the altimetry
 339 track (Huang et al., 2008), the T_0 and T_1 respectively represent the start and end
 340 observation time of the altimetry track. The correction v is used as the virtual
 341 observation to establish the error equation $v = f(t) + \delta$, δ is observation noise, and the
 342 unknown coefficients in $f(t)$ are solved by the least squares principle; finally, the
 343 solved coefficients and the measurement time t are put in the error model $f(t)$, and the
 344 SSH error of each observation point is calculated, and the SSH is corrected.

345 3.1.3 The mean sea level model establishing

346 The least squares collocation (LSC) method ~~are~~is excellent at achieving optimal
 347 interpolation using the priori information of observations (Jin et al., 2011). In this
 348 study, the LSC method is used to establish the mean sea level model on $5' \times 5'$ grids
 349 based on the along-track SSH data. The steps of this method are as follows: firstly, the
 350 geoid height calculated from the EGM2008 Global Gravity Field model is selected as
 351 the reference SSH, and the SSH data subtracts the reference SSH to obtain the
 352 residual SSH; then the along-track residual SSH is de-averaged, and gridded by
 353 applying the LSC method, where the covariance function in the LSC method is

354 described by a second-order Markov process (Jordan, 1972); finally, the average value
 355 of the residual SSH is added back to the grid value, and the reference SSH is also
 356 recovered, a mean sea level model on 5'×5' grids is established.

357 3.1.4 Long-term altimetry SLCR model establishing

358 ~~This study calculates nine mean sea level models using nine groups of SSH data,~~
 359 Nine mean sea level models are established in this study using nine groups of SSH
 360 data, which constructs sea level time series data with 1-year interval. Then, we apply
 361 the least squares method to estimate the long-term altimetry SLCR. The SDUST
 362 global altimetry SLCR model (SDUST_Altimetry_SLCR) on 5'×5' grids is
 363 established, and will be compared with the AVISO global altimetry SLCR model
 364 (AVISO_Altimetry_SLCR).

365 3.2 Estimation of steric SLCR

366 The changes in ocean temperature and salinity cause ~~the seawater volume~~
 367 changeocean volume changes, which are also known as steric SSH changes. The
 368 steric SSH change at any location can be calculated using the seawater density change
 369 (Llovel et al., 2010; Fofonoff and Millard, 1983):

~~$$370 \quad \Delta SSH_{Steric}(N, \lambda, \theta) = \frac{1}{\rho_S} \int_{-h}^0 \rho[(N, \lambda, \theta, z, T, S) - \bar{\rho}(\lambda, \theta, z, \bar{T}, \bar{S})] dz \quad (7)$$~~

$$371 \quad \Delta SSH_{Steric}(N, \lambda, \theta) = \frac{1}{\rho_S} \int_{-h}^0 \rho(N, \lambda, \theta, z, T, S) - \bar{\rho}(\lambda, \theta, z, \bar{T}, \bar{S}) dz \quad (7)$$

372 Where z represents the seawater depth, ρ , T and S are the density, temperature and
 373 salinity of seawater, $\bar{\rho}$, \bar{T} and \bar{S} are the average density, average temperature and
 374 average salinity of seawater from January 1993 to December 2019, h is the distance
 375 from the sea bottom to the sea surface.

376 This study utilizes the EN4.2.1 monthly ocean temperature and salinity data from
 377 January 1993 to December 2019 to calculate the monthly steric SSH changes on a
 378 1°×1° grid, and then applies the least squares model to estimate the long-term steric
 379 SLCR. Finally, the EN4 global steric SLCR model (EN4_Steric_SLCR) with 1°×1°
 380 grid size is constructed.

381 3.3 Estimation of mass-term SLCR

382 The altimetry sea level change represents the total sea level change, which
 383 includes ~~seawater volume change~~ocean volume change and seawater mass change
 384 (Yang et al., 2022). Therefore, the EN4 steric SLCR is subtracted from the SDUST
 385 altimetry SLCR:

$$386 \quad SLCR_{Mass} = SLCR_{Altimetry} - SLCR_{Steric} \quad (8)$$

387 Note that the EN4 steric SLCR model, initially defined on $1^\circ \times 1^\circ$ grids, is up-sampled
 388 to $5' \times 5'$ using the Kriging interpolation model to facilitate model calculation. Finally,
 389 the SDUST global mass-term SLCR model (SDUST_Mass_SLCR) with $5' \times 5'$ grid
 390 size is constructed, which will be compared with the GRACE/GRACE-FO mass-term
 391 SLCR model.

392 3.4 Estimation of MGCR

393 The Earth ~~have~~ has an obvious load response to the surface mass change, ~~the~~
 394 ~~load response includes Earth surface displacement and gravity field change. This load~~
 395 ~~response manifests as Earth's surface displacement and gravity field change.~~ The
 396 Earth's gravity field change by the mass load response can be calculated by applying
 397 the spherical harmonic function method. The spherical harmonic function method can
 398 be divided into two steps: the spherical harmonic analysis and spherical harmonic
 399 synthesis (Sneeuw, 1994; Godah, 2019).

400 Firstly, the global mass-term SLCR is expanded into spherical harmonic
 401 coefficients:

$$402 \quad \left\{ \begin{array}{l} \dot{\bar{C}}_{lm}^{Mass} = \frac{1}{4\pi a} \cdot \frac{3\rho_0}{\rho_{ave}} \cdot \frac{(1+k_l)}{(2l+1)} \cdot \int_0^{2\pi} \int_0^\pi SLCR_{Mass}(\lambda, \theta) \cdot \bar{P}_{lm}(\cos \theta) \cdot \\ \cos m\lambda \cdot \sin \theta d\theta d\lambda \\ \dot{\bar{S}}_{lm}^{Mass} = \frac{1}{4\pi a} \cdot \frac{3\rho_0}{\rho_{ave}} \cdot \frac{(1+k_l)}{(2l+1)} \cdot \int_0^{2\pi} \int_0^\pi SLCR_{Mass}(\lambda, \theta) \cdot \bar{P}_{lm}(\cos \theta) \cdot \\ \sin m\lambda \cdot \sin \theta d\theta d\lambda \end{array} \right. \quad (9)$$

$$403 \quad \left\{ \begin{array}{l} \dot{\bar{C}}_{lm}^{Mass} = (1/4\pi a) \cdot (3\rho_0 / \rho_{ave}) \cdot [(1+k_l) / (2l+1)] \cdot \\ \int_0^{2\pi} \int_0^\pi SLCR_{Mass}(\lambda, \theta) \cdot \bar{P}_{lm}(\cos \theta) \cdot \cos m\lambda \cdot \sin \theta d\theta d\lambda \\ \dot{\bar{S}}_{lm}^{Mass} = (1/4\pi a) \cdot (3\rho_0 / \rho_{ave}) \cdot [(1+k_l) / (2l+1)] \cdot \\ \int_0^{2\pi} \int_0^\pi SLCR_{Mass}(\lambda, \theta) \cdot \bar{P}_{lm}(\cos \theta) \cdot \sin m\lambda \cdot \sin \theta d\theta d\lambda \end{array} \right. \quad (9)$$

404 Where $\dot{\bar{C}}_{lm}^{Mass}$ and $\dot{\bar{S}}_{lm}^{Mass}$ are the fully normalized geopotential annual trend coefficients
 405 corresponding to the mass-term SLCR. The grid size of the SDUST mass-term SLCR

406 model is $5' \times 5'$, so its spherical harmonic coefficient is fully calculated to ~~the~~ 2160
 407 degree. The above process is called spherical harmonic analysis.

408 In order to deduct the GIA effect, this study subtracts the GIA corrected
 409 geopotential annual trend coefficients $\dot{\bar{C}}_{lm}^{GIA}$ and $\dot{\bar{S}}_{lm}^{GIA}$ from $\dot{\bar{C}}_{lm}^{Mass}$ and $\dot{\bar{S}}_{lm}^{Mass}$:

$$410 \quad \begin{cases} \dot{\bar{C}}_{lm} = \dot{\bar{C}}_{lm}^{Mass} - \dot{\bar{C}}_{lm}^{GIA} \\ \dot{\bar{S}}_{lm} = \dot{\bar{S}}_{lm}^{Mass} - \dot{\bar{S}}_{lm}^{GIA} \end{cases} \quad (10)$$

411 Then according to the spherical harmonic coefficient and the position information, the
 412 spherical harmonic domain integration is performed:

$$413 \quad MGCR(r, \lambda, \theta) = \frac{GM}{r^2} \sum_{l=0}^{2160} \sum_{m=0}^l (l-1)(a/r)^l \bar{P}_{lm}(\cos \theta) (\dot{\bar{C}}_{lm} \cos m\lambda + \dot{\bar{S}}_{lm} \sin m\lambda) \quad (11)$$

414 The above calculation is also called spherical harmonic synthesis. The SDUST
 415 global MGCR model (SDUST2020MGCR) with a grid size of $5' \times 5'$ is obtained using
 416 the spherical harmonic coefficient of degree 2160. The SDUST2020MGCR will be
 417 compared with the GRACE/GRACE-FO MGCR model (GRACE2020MGCR).

418 **4 Results and analysis**

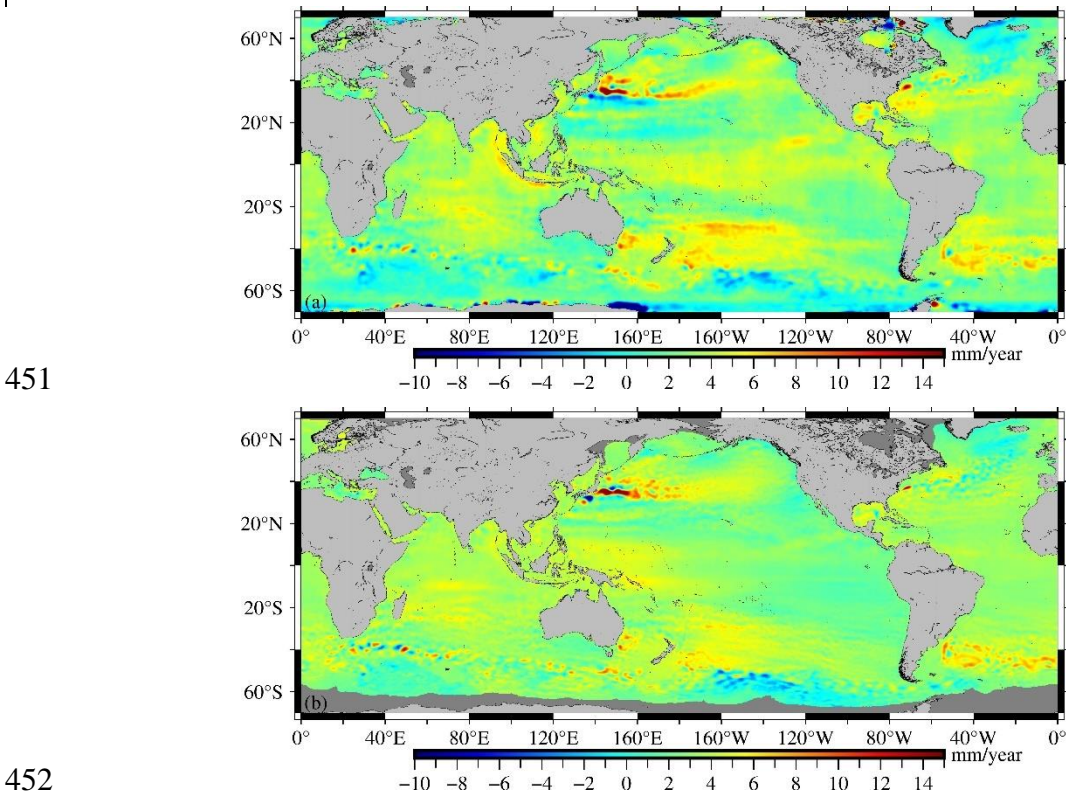
419 This study calculates the long-term SLCR of the sea area covering 70°S - 70°N ,
 420 and finally obtains the long-term MGCR. The grid sizes of models in the study are
 421 inconsistent. Therefore, to enhance the presentation of models for comparison, the
 422 models with grid sizes smaller than $5' \times 5'$ ~~is~~ are up-sampled to $5' \times 5'$ applying the
 423 Kriging interpolation method. The results are discussed and analyzed below.

424 **4.1 The SLCR model**

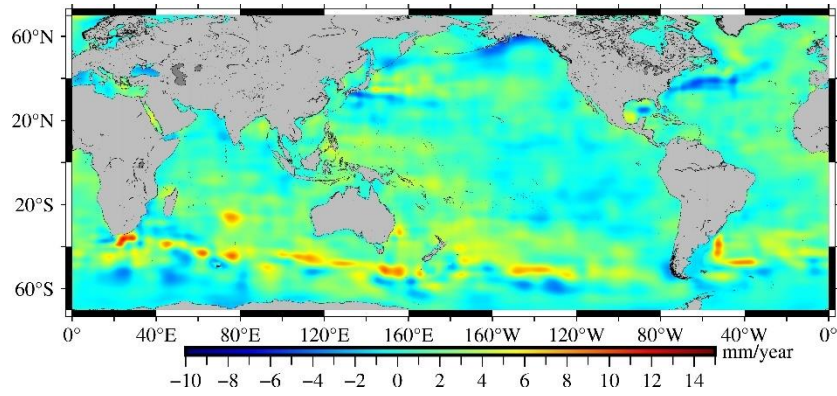
425 The SDUST_Altimetry_SLCR constructed by using multi-L2P satellite altimetry
 426 data is shown in Fig. 4a. The AVISO_Altimetry_SLCR constructed by using AVISO
 427 monthly sea level anomaly data is shown in Fig. 4b. The Fig. 5 illustrates
 428 EN4_Steric_SLCR, which is constructed using EN4.2.1 ocean temperature and
 429 salinity data. Furthermore, The SDUST_Mass_SLCR obtained by subtracting
 430 EN4_Steric_SLCR from SDUST_Altimetry_SLCR is shown in Fig. 6a, and the
 431 GRACE_Mass_SLCR resolved from the GRACE/GRACE-FO monthly geopotential
 432 spherical harmonic data is presented in Fig. 6b. Upon comparing the results of long-
 433 term altimetry SLCR (Fig. 4), it is evident that the distribution characteristics of the
 434 SDUST_Altimetry_SLCR and the AVISO_Altimetry_SLCR are basically consistent
 435 on the global scale. Upon comparing the results of the long-term mass-term SLCR

436 (Fig. 6a and Fig. 6b), there are some differences in the distribution characteristics of
437 SDUST_Mass_SLCR and GRACE_Mass_SLCR on the global scale, however,
438 similarities are identified in local sea areas, such as the eastern seas of Japan, the
439 western seas of the Nicobar Islands, and the southern seas of Greenland.

440 The variation of terrestrial water storage is unevenly distributed in space. This
441 uneven variation of mass will in turn load the Earth and cause the sea level change,
442 these effects are termed self-attraction and loading (SAL) (Tamisiea et al., 2010).
443 Based on the method proposed by Sun et al. (2019), the GRACE/GRACE-FO data
444 and the fingerprints of mass redistributions (fingerprint is a base function associated
445 with a particular spatial mass distribution) are used, and the sea level equation on an
446 elastic Earth is solved. The SAL effect is estimated, and the result is shown in Fig. 6c.
447 The melting of the Greenland ice sheet due to global warming has reduced terrestrial
448 water storage (Groh et al., 2019). By comparing Fig. 6 (a), (b), (c), the results reflect
449 the correlation between mass-term sea level decline in southern Greenland and a
450 reduction in Greenland terrestrial water storage.

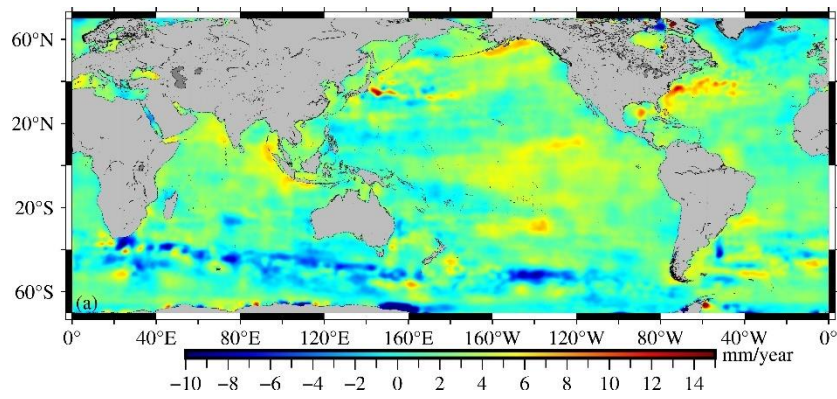


453 Figure 4. The long-term altimetry SLCR. (a) SDUST_Altimetry_SLCR, (b)
454 AVISO_Altimetry_SLCR.

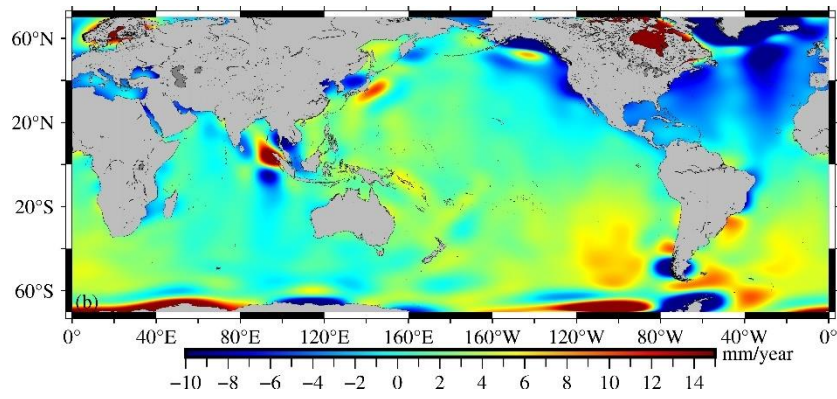


455

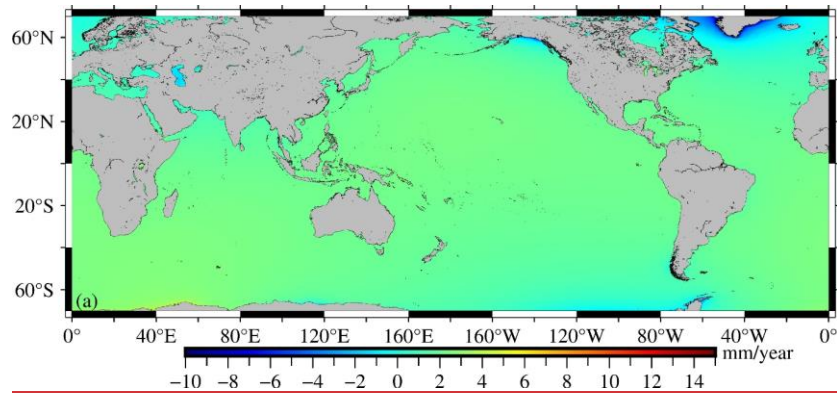
456 Figure 5. The long-term steric SLCR (EN4_Steric_SLCR).



457



458



459

460 Figure 6. The long-term mass-term SLCR. (a) SDUST_Mass_SLCR, (b) GRACE_Mass_SLCR, (c)

461 (c) The SLCR caused by self-attraction and loading effect

462 The long-term SLCR for the global ocean (60°S~60°N), the Indian Ocean
 463 (20°~105°E, 60°S~30°N), the Pacific Ocean (105°E~80°W, 60°S~60°N) and the

464 Atlantic Ocean (80°W~20°E, 60°S~60°N) are statistically analyzed, and the results
 465 are shown in Table 1. The statistical results of SDUST_Altimetry_SLCR and
 466 AVISO_Altimetry_SLCR are basically consistent, and the mean value of altimetry
 467 SLCR in the global ocean is ~~all~~ about 3.2 mm/year. The results of previous studies
 468 show that the mean value of global SLCR is about 3 mm/year (Leuliette and Miller,
 469 2009; Cazenave et al., 2014), which is further confirmed by the SLCR results of this
 470 study. There are some differences in the statistical results of SDUST_Mass_SLCR
 471 and GRACE_Mass_SLCR, but the mean values for both are all positive, signifying an
 472 overall upward trend in the mass-term sea level. In addition, the statistical results
 473 show that the standard deviation (STD) of SDUST_Mass_SLCR is smaller than
 474 GRACE_Mass_SLCR. The more detailed comparative analysis of the results derived
 475 from ~~multi~~-L2P satellite altimetry and GRACE/GRACE-FO is presented in Sect. 4.2.

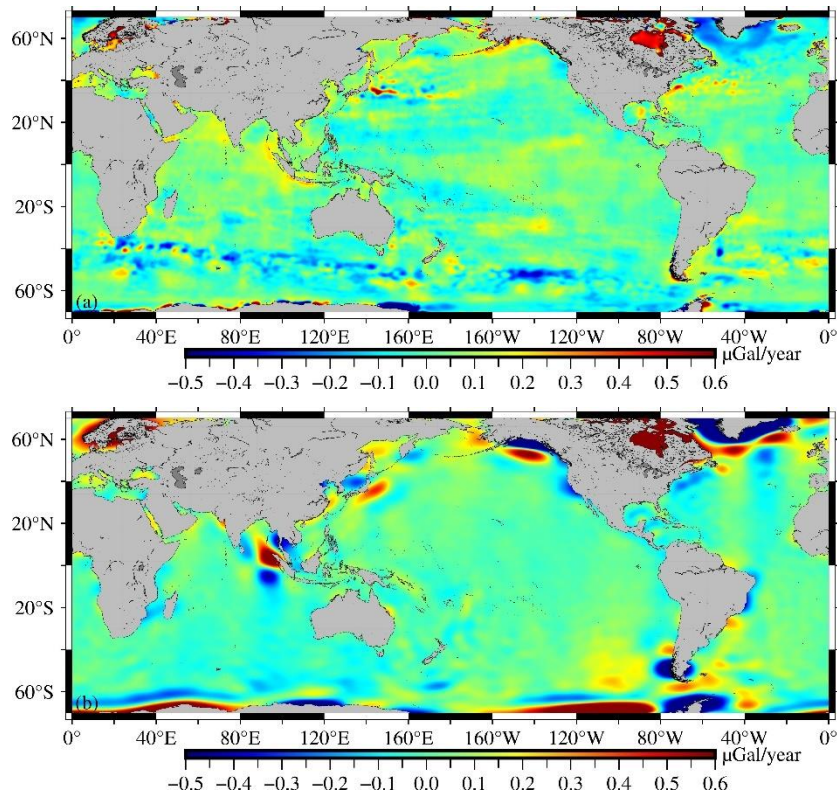
476 Table 1. Statistical results of long-term SLCR (mm/year)

SLCR Models	Oceans	Max	Min	Mean	STD
SDUST_Altimetry_SLCR	Global	25.75	-9.66	3.18	1.59
	Indian	13.08	-4.69	3.04	1.65
	Pacific	25.75	-9.66	3.22	1.65
	Atlantic	16.05	-9.07	3.21	1.39
AVISO_Altimetry_SLCR	Global	30.28	-15.55	3.22	1.38
	Indian	14.06	-5.72	3.41	1.25
	Pacific	30.28	-15.55	3.15	1.52
	Atlantic	16.77	-2.55	3.25	1.13
EN4_Steric_SLCR	Global	11.72	-5.94	1.19	1.72
	Indian	11.72	-3.87	1.33	1.97
	Pacific	9.58	-5.94	1.17	1.71
	Atlantic	9.72	-5.01	1.13	1.54
SDUST_Mass_SLCR	Global	16.53	-11.52	1.98	1.98
	Indian	9.57	-11.52	1.70	2.27
	Pacific	16.53	-10.10	2.03	1.97
	Atlantic	14.10	-9.71	2.06	1.75
GRACE_Mass_SLCR	Global	44.43	-85.54	1.16	4.46
	Indian	24.03	-12.42	0.69	2.63
	Pacific	42.90	-85.54	1.75	4.45
	Atlantic	44.43	-53.19	0.27	5.18

477 4.2 The MGCR model

478 The SDUST2020MGCR constructed by applying the spherical harmonic
 479 function method is shown in Fig. 7a, and the GRACE2020MGCR resolved from the
 480 GRACE/GRACE-FO satellite gravity data is shown in Fig. 7b. The
 481 SDUST2020MGCR and GRACE2020MGCR have similar spatial distribution
 482 characteristics in some local sea areas. In the eastern seas of Japan, both

483 SDUST2020MGCR and GRACE2020MGCR can detect the dipole phenomenon of
 484 marine gravity change, which may be related to the gradually increasing ocean
 485 circulation (Wang and Wu, 2019). Although the position and range of the dipole are
 486 not completely consistent, both the altimetry and GRACE results can reflect the
 487 impact of intensified ocean currents on the marine gravity field. The Nicobar Islands
 488 in the northeastern Indian Ocean are located on the collision boundary where the
 489 oceanic plate subducts beneath the continental plate. Both SDUST2020MGCR and
 490 GRACE2020MGCR indicate that the marine gravity in the western seas of the
 491 Nicobar Islands is rising, which may be attributed to the material accumulation caused
 492 by plate subduction (Zhu et al., 2023). In the southern seas of Greenland, both
 493 SDUST2020MGCR and GRACE2020MGCR exhibit a downward trend, which is
 494 related to the mass loss of Greenland due to ice melting (Groh et al., 2019). In the seas
 495 near the West Wind Drift and the Brazilian Warm Current, both SDUST2020MGCR
 496 and GRACE2020MGCR reveal that the high-frequency signals of marine gravity
 497 changes are relatively significant, which reflects the influence of ocean currents on
 498 the marine gravity field (Zhang et al., 2021; Zhu et al., 2022). However, differences
 499 exist in the global scale spatial distribution between SDUST2020MGCR and
 500 GRACE2020MGCR. The Fig. 7a shows that GRACE2020MGCR still exhibits strip
 501 noise and may contains leakage errors residuals.



504 Figure 7. The long-term MGCR. (a) SDUST2020MGCR, (b) GRACE2020MGCR.

505 The long-term MGCR in the global ocean, the Indian Ocean, the Pacific Ocean
506 and the Atlantic Ocean are statistically analyzed, and the results are presented in Table

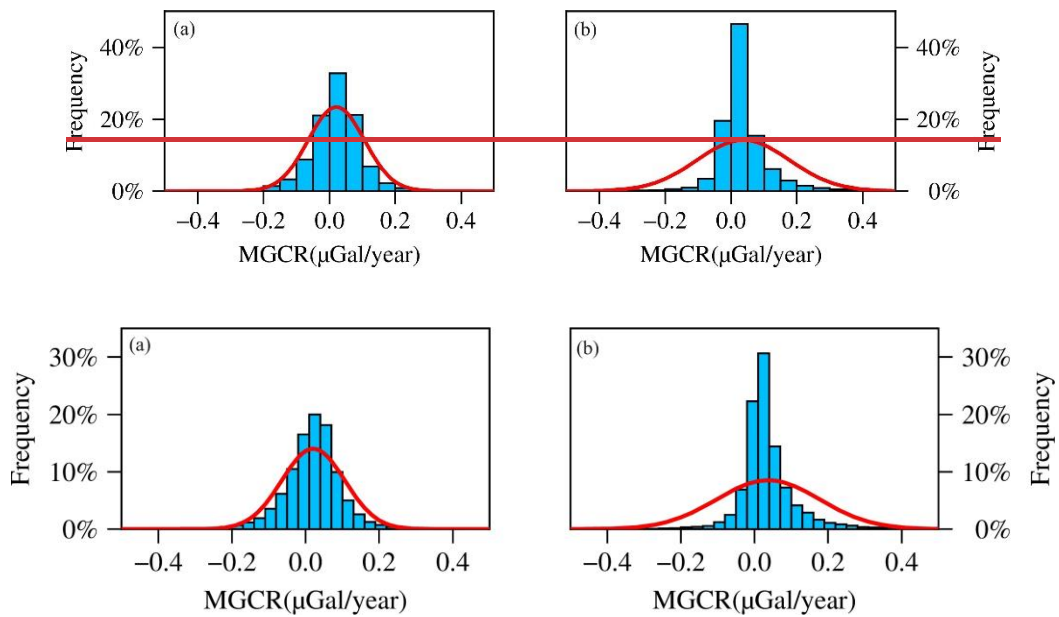
507 ~~2. The statistical histogram of the long-term MGCR is plotted, as shown in Fig. 8. The~~
508 ~~power spectral density of MGCR model is estimated by using the periodogram~~
509 ~~method, as illustrated in Fig. 9. The~~ Table 2 shows that the long-term MGCR mean
510 values for both SDUST2020MGCR and GRACE2020MGCR are positive values in
511 the global and local oceans. The long-term MGCR mean value in global ocean is
512 about 0.02 $\mu\text{Gal}/\text{year}$. The statistical results also indicate that the STD of
513 SDUST2020MGCR is smaller than GRACE2020MGCR. The processed GRACE data
514 still have strip noise residuals and signal leakage error residuals (Chen et al., 2014),
515 the large STD of GRACE MGCR may be related to these error residuals. Strip noise,
516 leakage errors and their residuals affect the true physical signal, so the GRACE time-
517 varying marine gravity used for comparison is not precise. In the process of solving
518 the mean sea level using the along-track altimetry data, the altimetry data were
519 preprocessed (such as 19-year moving grouping, collinear adjustment, space-time
520 objective analysis interpolation, and crossover adjustment) to eliminate the influence
521 of anomalous ocean variability and some residuals, so that the STD of the SDUST
522 MGCR is smaller. The Fig. 8 shows that the MGCR value of SDUST2020MGCR and
523 GRACE2020MGCR are mainly between -0.2 and 0.2 $\mu\text{Gal}/\text{year}$, and
524 SDUST2020MGCR is more consistent with the Gaussian normal distribution. The Fig.
525 9 shows that the signal strength of SDUST2020MGCR is greater than
526 GRACE2020MGCR in the entire frequency domain.

527 Table 42. Statistical results of long-term MGCR ($\mu\text{Gal}/\text{year}$)

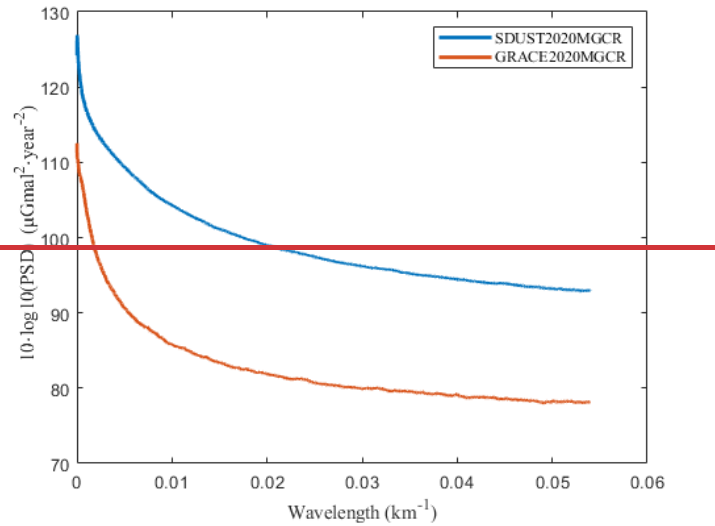
	Oceans	Max	Min	Mean	STD
SDUST2020MGCR	Global	3.28	-1.41	0.02	0.09
	Indian	0.47	-0.44	0.03	0.08
	Pacific	1.37	-0.48	0.02	0.08
	Atlantic	3.28	-1.41	0.03	0.09
GRACE2020MGCR	Global	1.00	-3.60	0.03	0.14
	Indian	1.00	-0.51	0.01	0.10
	Pacific	0.95	-3.60	0.03	0.14
	Atlantic	0.94	-1.52	0.06	0.15

528 The statistical histogram of the long-term MGCR is plotted, as shown in Fig. 8.
529 The Fig. 8 shows that the MGCR value of SDUST2020MGCR and
530 GRACE2020MGCR are mainly between -0.2 and 0.2 $\mu\text{Gal}/\text{year}$, and
531 SDUST2020MGCR is more consistent with the Gaussian normal distribution.

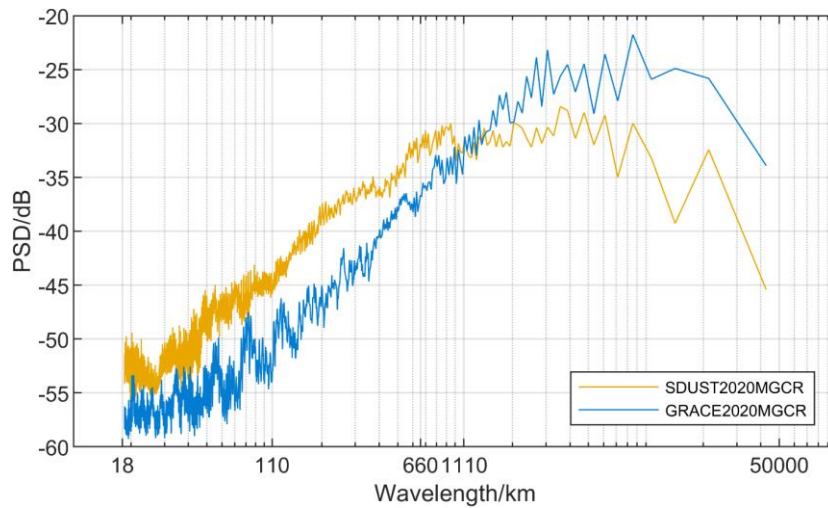
532 Utilizing the periodogram method, the power spectral density of MGCR model is
 533 estimated, and the result is illustrated in Fig. 9. The vertical axis of Fig. 9 is scaled by
 534 a factor of $10\lg$, the horizontal axis is wavelength. In this study, the
 535 GRACE2020MGCR was constructed using the GRACE model of spherical harmonic
 536 degree 60. The spherical harmonic degree can be calculated from wavelength using
 537 the conversion formula $40000/\text{wavelength}$. The Fig. 9 shows that when the
 538 wavelength exceeds 1110 km, corresponding to a spherical harmonic degree less than
 539 36, the signal strength of GRACE2020MGCR is greater than SDUST2020MGCR.
 540 When the wavelength is greater than 660 km and less than 1110 km, corresponding to
 541 a spherical harmonic degree greater than 36 and less than 60, the signal strength of
 542 GRACE2020MGCR is lower than SDUST2020MGCR, which suggests that it is
 543 possible to improve the GRACE model of spherical harmonic degree 60 by using
 544 altimetry data. When the wavelength is less than 660 km, the signal strength of
 545 SDUST2020MGCR remains greater than GRACE2020MGCR.



547
 548 Figure 8. The statistical histogram of the long-term MGCR. (a) SDUST2020MGCR, (b)
 549 GRACE2020MGCR.



550



551

552 Figure 9. The power spectral density of MGCR model.

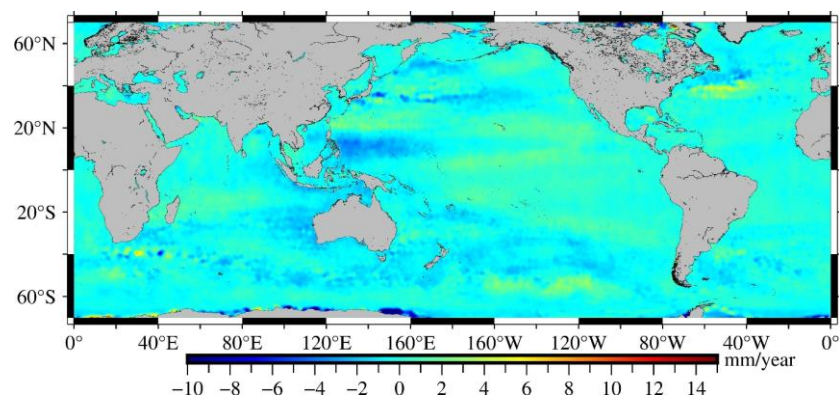
553 There are some differences in spatial distribution and statistical results between
 554 SDUST2020MGCR and GRACE2020MGCR, which are mainly related to the
 555 following factors: (1) The spatial resolution of the GRACE/GRACE-FO monthly
 556 gravity data is low, its signal contains north-south strip noise and leakage errors, and
 557 both error correction processing and error residuals make real geophysical signals
 558 distorted and weak. (2) The satellite altimetry data exhibits relatively high spatial
 559 resolution, but its time-varying marine gravity may be affected by SSH measurement
 560 errors. (3) The EN4.2.1 ocean temperature and salinity data suffer accuracy problems
 561 that arise from irregular spatial data distribution and model gridding. Consequently,
 562 the spatial distribution and statistics of SDUST2020MGCR and GRACE2020MGCR
 563 are challenging to mutually validate.

564 **4.3 Reliability analysis of model**

565 In many previous studies, there is a problem that the independent observations of

566 GRACE satellite and altimetry satellite do not match well in terms of spatial
567 resolution and observation accuracy, the GRACE and altimetry results are difficult to
568 verify each other (Willis et al., 2008; Feng et al., 2014). Therefore, it is not possible to
569 use the GRACE results to assess the reliability of the altimetry results. In this study,
570 we conducted a reliability analysis aimed at informing potential dataset users about
571 regions where reliability is diminished.

572 We split the altimetry data in half, use data groups 1-5 to estimate SLCR1 and
573 data groups 5-9 to estimate SLCR2, and then calculate the difference between the two
574 SLCR, and the result is depicted in Figure 10. Where SLCR differ substantially, the
575 reliability of altimetry results may be reduced. The results of Figure 10 show that the
576 noise from altimetry observations has little effect on SLCR in most global ocean areas.
577 The large SLCR differences are mainly observed near the ocean current areas. On the
578 one hand, the quality of altimetry data is poor in regions with strong ocean currents
579 (Vignudelli et al., 2006; Zhu et al., 2022), especially the West Wind Drift, and the
580 reliability of altimetry SLCR may be low. On the other hand, global climate change
581 leads to changes in the intensity of ocean current activities (Du et al., 2019), which
582 objectively causes significant sea level changes near the ocean current areas. Indeed,
583 the SLCR is estimated applying the 19-year moving window method, which can
584 effectively mitigate the impact of ocean currents. In summary, SLCR can overcome
585 the influence of noise from altimetry observation, to further solve the relatively stable
586 and reliable MGCR.



587
588 Figure 10. Difference of altimetry SLCR between two periods.

589 **5 Data availability**

590 The global marine gravity change rate model (SDUST2020MGCR) can be
591 downloaded on the website of <https://zenodo.org/records/10098524> (Zhu et al.,
592 2023b). The dataset contains geospatial information (latitude, longitude) and marine

593 gravity change rates.

594 The global marine gravity change rate model (SDUST2020MGCR) can be
595 downloaded on the website of <https://zenodo.org/records/10701641> (Zhu et al., 2024).

596 In this study, the GIA effect is deducted as a known factor, and thus the marine gravity
597 change rate is investigated for other factors. In fact, many science applications that
598 require mass change trends over the oceans would require both ocean mass signals
599 and solid Earth effects (GIA effects and seismic deformations). Therefore, the dataset
600 contains geospatial information (latitude, longitude), SDUST2020MGCR and an
601 attachment data (GIA MGCR). The users can sum the SDUST2020MGCR with the
602 GIA MGCR to obtain a full-signal MGCR, or if users do not want to consider the GIA
603 effects, they can just use the SDUST2020MGCR.

604 **6 Conclusions**

605 This study utilized multi-satellite altimetry data and ocean temperature-salinity
606 data from 1993 to 2019 to estimate the global mass-term SLCR. Based on the
607 spherical harmonic function method and mass load theory, we constructed the global
608 MGCR model (SDUST2020MGCR) on 5'×5' grids. This model provides ~~the~~ more
609 detailed information of changes in the marine gravity field.

610 The SDUST2020MGCR and the GRACE/GRACE-FO global MGCR model
611 (GRACE2020MGCR) were compared. In local sea areas where marine gravity
612 changes significantly, such as the eastern seas of Japan, the western seas of the
613 Nicobar Islands, and the southern seas of Greenland, the SDUST2020MGCR and
614 GRACE2020MGCR have certain similarities in spatial distribution. However, there
615 are some differences in the global spatial distribution between SDUST2020MGCR
616 and GRACE2020MGCR, which is mainly related to the mismatch in spatial
617 resolution among satellite altimetry data, satellite gravity data, and ocean temperature-
618 salinity data. Compared with the low-resolution GRACE2020MGCR, the
619 SDUST2020MGCR not only has a higher spatial resolution, but also excludes the
620 strip noise and leakage errors, so it can more realistically reflect the long-term
621 changes in the marine gravity field. The use of altimetry data can maximize the
622 opportunity to construct a high-resolution, high-precision MGCR model. Although the
623 altimetry MGCR may be less reliable at ocean current areas, the construction of
624 altimetry MGCR can fill the data gap compared to inability of GRACE to detect
625 small-scale marine gravity changes caused by ocean currents.

626 The marine gravity changes are mainly caused by the seawater mass changes: (1)
627 global warming leads to melting of glacier and ice sheet, sea level rise and seawater
628 mass increase, which in turn affects the global marine gravity field. (2) the climate
629 warming leads to change of ocean dynamics, such as changes in the intensity and
630 number of tropical cyclones and enhancement of ocean circulation, which causes
631 changes in the seawater mass distribution, and then affects the marine gravity field. (3)
632 The variation of terrestrial water storage is unevenly distributed in space, this
633 unevenly variation of mass will in turn load the Earth, named as self-attraction and
634 loading effect, which causes changes in seawater mass distribution, and consequently
635 changes in marine gravity. SDUST2020MGCR has higher spatial resolution and
636 excludes stripe noise and leakage errors, it can more realistically reflect the long-term
637 marine gravity change in more detail, which is meaningful for the study of seawater
638 mass migration and its associated geophysical processes.

639 ~~The marine gravity changes are the comprehensive result of mass migration in~~
640 ~~various layers of the Earth, such as the oceanosphere and lithosphere. Utilizing the~~
641 ~~high resolution MGCR model derived from multi satellite altimetry data, and~~
642 ~~integrating it with other Earth dataset, will be helpful to study the Earth material~~
643 ~~migration.~~

645 **Author contributions.**

646 FZ and JG designed the research and developed the algorithm. HZ downloaded
647 altimeter data and other data. FZ carried out the experimental results and wrote the
648 manuscript. LH, HS and XL gave related comments for this work.

649 **Competing interests.**

650 The contact author has declared that none of the authors has any competing interests.

651 **Disclaimer.**

652 Publisher's note: Copernicus Publications maintains neutrality regarding jurisdictional
653 claims in published maps and institutional affiliations.

654 **Acknowledgements.**

655 We appreciate AVISO for providing altimeter data and monthly sea level anomaly
656 data, the UK Met Office for contributing EN4.2.1 data, and the ICGEM for releasing
657 GRACE/GRACE-FO monthly geopotential spherical harmonics data. Special thanks
658 to Professors Peltier and Argus for sharing ICE-6G GIA model. Finally, we would

659 also like to thank the Generic Mapping Tools and its contributors.

660 **Financial support.**

661 This study receives partial support from the National Natural Science Foundation of
662 China (grant Nos. 42192535, 42274006 and 42242015), the Autonomous and
663 Controllable Project for Surveying and Mapping of China (grant No. 816-517), and
664 the Shandong University of Science and Technology Research Fund (grants No.
665 2014TDJH101).

666 **References**

- 667 Andersen, O. B. and Knudsen, P.: The DTU17 Global Marine Gravity Field: First
668 Validation Results, in: Fiducial Reference Measurements for Altimetry, Cham, 83–87,
669 https://doi.org/10.1007/1345_2019_65, 2020.
- 670 Andersen, O. B., Abulaitjiang, A., Zhang, S., and Rose, S. K.: A new high resolution
671 Mean Sea Surface (DTU21MSS) for improved sea level monitoring, Copernicus
672 Meetings, <https://doi.org/10.5194/egusphere-egu21-16084>, 2021.
- 673 Andersen, O. B., Rose, S. K., Abulaitjiang, A., Zhang, S., and Fleury, S.: The DTU21
674 Global Mean Sea Surface and First Evaluation, ESSD – Ocean/Physical oceanography,
675 <https://doi.org/10.5194/essd-2023-160>, 2023.
- 676 Argus, D. F., Peltier, W. R., Drummond, R., and Moore, A. W.: The Antarctica
677 component of postglacial rebound model ICE-6G_C (VM5a) based on GPS
678 positioning, exposure age dating of ice thicknesses, and relative sea level histories,
679 *Geophysical Journal International*, 198, 537–563, <https://doi.org/10.1093/gji/ggu140>,
680 2014.
- 681 Cazenave, A., Dieng, H.-B., Meyssignac, B., Von Schuckmann, K., Decharme, B., and
682 Berthier, E.: The rate of sea-level rise, *Nature Clim Change*, 4, 358–361,
683 <https://doi.org/10.1038/nclimate2159>, 2014.
- 684 Chen, J., Li, J., Zhang, Z., and Ni, S.: Long-term groundwater variations in Northwest
685 India from satellite gravity measurements, *Global and Planetary Change*, 116, 130–
686 138, <https://doi.org/10.1016/j.gloplacha.2014.02.007>, 2014.
- 687 CNES: Along-track Level-2+ (L2P) SLA Product Handbook, SALP-MU-P-EA-
688 23150-CLS, Issue 2.0,
689 [https://www.aviso.altimetry.fr/fileadmin/documents/data/tools/hdbk_L2P_all_mission
690 s_except_S3.pdf](https://www.aviso.altimetry.fr/fileadmin/documents/data/tools/hdbk_L2P_all_missions_except_S3.pdf) (last access: 6 November 2023), 2020.
- 691 Du, Y., Zhang, Y., and Shi, J.: Relationship between sea surface salinity and ocean
692 circulation and climate change, *Sci. China Earth Sci.*, 62, 771–782,
693 <https://doi.org/10.1007/s11430-018-9276-6>, 2019.
- 694 Ducet, N., Le Traon, P. Y., and Reverdin, G.: Global high-resolution mapping of ocean
695 circulation from TOPEX/Poseidon and ERS-1 and -2, *J. Geophys. Res.*, 105, 19477–
696 19498, <https://doi.org/10.1029/2000JC900063>, 2000.
- 697 Feng W., Zhong M., and Xu H.: Global sea level changes estimated from satellite
698 altimetry, satellite gravimetry and Argo data during 2005-2013, *Prog. Geophys.*, 29,

699 471–477, 2014.

700 Flechtner, F., Reigber, C., Rummel, R., and Balmino, G.: Satellite Gravimetry: A
701 Review of Its Realization, *Surv Geophys*, 42, 1029–1074,
702 <https://doi.org/10.1007/s10712-021-09658-0>, 2021.

703 Flury, J. and Rummel, R. (Eds.): Future satellite gravimetry and earth dynamics,
704 Springer, Dordrecht, 163 pp., 2005.

705 Fofonoff, N. and Millard, R.: Algorithms for computation of fundamental properties
706 of seawater, In UNESCO technical papers in marine science, 44, 1983.

707 Godah, W.: IGIK–TVGMF: A MATLAB package for computing and analysing
708 temporal variations of gravity/mass functionals from GRACE satellite based global
709 geopotential models, *Computers & Geosciences*, 123, 47–58,
710 <https://doi.org/10.1016/j.cageo.2018.11.008>, 2019.

711 Good, S. A., Martin, M. J., and Rayner, N. A.: EN4: Quality controlled ocean
712 temperature and salinity profiles and monthly objective analyses with uncertainty
713 estimates: THE EN4 DATA SET, *J. Geophys. Res. Oceans*, 118, 6704–6716,
714 <https://doi.org/10.1002/2013JC009067>, 2013.

715 Gopalapillai, G. S. and Mourad, A. G.: Detailed gravity anomalies from Geos 3
716 satellite altimetry data, *J. Geophys. Res.*, 84, 6213–6218,
717 <https://doi.org/10.1029/JB084iB11p06213>, 1979.

718 Greco, F., Currenti, G., D’Agostino, G., Germak, A., Napoli, R., Pistorio, A., and Del
719 Negro, C.: Combining relative and absolute gravity measurements to enhance volcano
720 monitoring, *Bull Volcanol*, 74, 1745–1756, [https://doi.org/10.1007/s00445-012-0630-](https://doi.org/10.1007/s00445-012-0630-0)
721 0, 2012.

722 Groh, A., Horwath, M., Horvath, A., Meister, R., Sørensen, L. S., Barletta, V. R.,
723 Forsberg, R., Wouters, B., Ditmar, P., Ran, J., Klees, R., Su, X., Shang, K., Guo, J.,
724 Shum, C. K., Schrama, E., and Shepherd, A.: Evaluating GRACE Mass Change Time
725 Series for the Antarctic and Greenland Ice Sheet—Methods and Results, *Geosciences*,
726 9, 415, <https://doi.org/10.3390/geosciences9100415>, 2019.

727 Han, S.-C., Jekeli, C., and Shum, C. K.: Time-variable aliasing effects of ocean tides,
728 atmosphere, and continental water mass on monthly mean GRACE gravity field:
729 TEMPORAL ALIASING ON GRACE GRAVITY FIELD, *J. Geophys. Res.*, 109,
730 <https://doi.org/10.1029/2003JB002501>, 2004.

731 Hosoda, S., Ohira, T., and Nakamura, T.: A monthly mean dataset of global oceanic
732 temperature and salinity derived from Argo float observations, *JAMSTEC-R*, 8, 47–
733 59, <https://doi.org/10.5918/jamstecr.8.47>, 2008.

734 Huang, M., Zhai, G., Ouyang, Y., Lu, X., Liu, C., and Wang, R.: Integrated Data
735 Processing for Multi-Satellite Missions and Recovery of Marine Gravity Field, *Terr.*
736 *Atmos. Ocean. Sci.*, 19, 103, [https://doi.org/10.3319/TAO.2008.19.1-2.103\(SA\)](https://doi.org/10.3319/TAO.2008.19.1-2.103(SA)), 2008.

737 Hwang, C., Hsu, H.-Y., and Jang, R.-J.: Global mean sea surface and marine gravity
738 anomaly from multi-satellite altimetry: applications of deflection-geoid and inverse
739 Vening Meinesz formulae, *Journal of Geodesy*, 76, 407–418,
740 <https://doi.org/10.1007/s00190-002-0265-6>, 2002.

741 Jin, T., Li, J., Jiang, W., and Wang, Z.: The new generation of global mean sea surface
742 height model based on multi-altimetric data, *Acta Geodaetica et Cartographica Sinica*,
743 40, 723–729, 2011.

744 Jordan, S. K.: Self-consistent statistical models for the gravity anomaly, vertical
745 deflections, and undulation of the geoid, *J. Geophys. Res.*, 77, 3660–3670,
746 <https://doi.org/10.1029/JB077i020p03660>, 1972.

747 Leuliette, E. W. and Miller, L.: Closing the sea level rise budget with altimetry, Argo,
748 and GRACE, *Geophysical Research Letters*, 36, 2008GL036010,
749 <https://doi.org/10.1029/2008GL036010>, 2009.

750 Li, Q., Bao, L., and Shum, C. K.: Altimeter-derived marine gravity variations reveal
751 the magma mass motions within the subaqueous Nishinoshima volcano, Izu–Bonin
752 Arc, Japan, *J Geod*, 95, 46, <https://doi.org/10.1007/s00190-021-01488-7>, 2021.

753 Liang, W., Zhang, G., Zhu, Y., Xu, Y., Guo, S., Zhao, Y., Liu, F., and Zhao, L.: Gravity
754 variations before the Menyuan Ms 6.4 earthquake, *Geodesy and Geodynamics*, 7,
755 223–229, <https://doi.org/10.1016/j.geog.2016.04.013>, 2016.

756 Llovel, W., Guinehut, S., and Cazenave, A.: Regional and interannual variability in
757 sea level over 2002–2009 based on satellite altimetry, Argo float data and GRACE
758 ocean mass, *Ocean Dynamics*, 60, 1193–1204, [https://doi.org/10.1007/s10236-010-](https://doi.org/10.1007/s10236-010-0324-0)
759 0324-0, 2010.

760 Nerem, R. S., Chambers, D. P., Choe, C., and Mitchum, G. T.: Estimating Mean Sea
761 Level Change from the TOPEX and Jason Altimeter Missions, *Marine Geodesy*, 33,
762 435–446, <https://doi.org/10.1080/01490419.2010.491031>, 2010.

763 Peltier, W. R., Argus, D. F., and Drummond, R.: Space geodesy constrains ice age
764 terminal deglaciation: The global ICE-6G_C (VM5a) model, *JGR Solid Earth*, 120,
765 450–487, <https://doi.org/10.1002/2014JB011176>, 2015.

766 Rapp, R. H., Yi, Y., and Wang, Y. M.: Mean sea surface and geoid gradient
767 comparisons with TOPEX altimeter data, *J. Geophys. Res.*, 99, 24657–24667,
768 <https://doi.org/10.1029/94JC00918>, 1994.

769 Riser, S. C., Freeland, H. J., Roemmich, D., Wijffels, S., Troisi, A., Belbéoch, M.,
770 Gilbert, D., Xu, J., Pouliquen, S., Thresher, A., Le Traon, P.-Y., Maze, G., Klein, B.,
771 Ravichandran, M., Grant, F., Poulain, P.-M., Suga, T., Lim, B., Sterl, A., Sutton, P.,
772 Mork, K.-A., Vélez-Belchí, P. J., Ansorge, I., King, B., Turton, J., Baringer, M., and
773 Jayne, S. R.: Fifteen years of ocean observations with the global Argo array, *Nature*
774 *Clim Change*, 6, 145–153, <https://doi.org/10.1038/nclimate2872>, 2016.

775 Roemmich, D. and Gilson, J.: The 2004–2008 mean and annual cycle of temperature,
776 salinity, and steric height in the global ocean from the Argo Program, *Progress in*
777 *Oceanography*, 82, 81–100, <https://doi.org/10.1016/j.pocean.2009.03.004>, 2009.

778 Sandwell, D., Garcia, E., Soofi, K., Wessel, P., Chandler, M., and Smith, W. H. F.:
779 Toward 1-mGal accuracy in global marine gravity from CryoSat-2, Envisat, and
780 Jason-1, *The Leading Edge*, 32, 892–899, <https://doi.org/10.1190/tle32080892.1>, 2013.

781 Sandwell, D. T., Harper, H., Tozer, B., and Smith, W. H. F.: Gravity field recovery
782 from geodetic altimeter missions, *Advances in Space Research*, 68, 1059–1072,

783 <https://doi.org/10.1016/j.asr.2019.09.011>, 2021.

784 Schaeffer, P., Faugère, Y., Legeais, J. F., Ollivier, A., Guinle, T., and Picot, N.: The
785 CNES_CLS11 Global Mean Sea Surface Computed from 16 Years of Satellite
786 Altimeter Data, *Marine Geodesy*, 35, 3–19,
787 <https://doi.org/10.1080/01490419.2012.718231>, 2012.

788 Sneeuw, N.: Global spherical harmonic analysis by least-squares and numerical
789 quadrature methods in historical perspective, *Geophysical Journal International*, 118,
790 707–716, <https://doi.org/10.1111/j.1365-246X.1994.tb03995.x>, 1994.

791 Sun, Y., Riva, R., Ditmar, P., and Rietbroek, R.: Using GRACE to Explain Variations
792 in the Earth’s Oblateness, *Geophysical Research Letters*, 46, 158–168,
793 <https://doi.org/10.1029/2018GL080607>, 2019.

794 Taburet, G., Sanchez-Roman, A., Ballarotta, M., Pujol, M.-I., Legeais, J.-F., Fournier,
795 F., Faugere, Y., and Dibarboue, G.: DUACS DT2018: 25 years of reprocessed sea
796 level altimetry products, *Ocean Sci.*, 15, 1207–1224, [https://doi.org/10.5194/os-15-](https://doi.org/10.5194/os-15-1207-2019)
797 1207-2019, 2019.

798 Tamisiea, M. E., Hill, E. M., Ponte, R. M., Davis, J. L., Velicogna, I., and
799 Vinogradova, N. T.: Impact of self-attraction and loading on the annual cycle in sea
800 level, *J. Geophys. Res.*, 115, 2009JC005687, <https://doi.org/10.1029/2009JC005687>,
801 2010.

802 Tapley, B. D., Bettadpur, S., Ries, J. C., Thompson, P. F., and Watkins, M. M.:
803 GRACE Measurements of Mass Variability in the Earth System, *Science*, 305, 503–
804 505, <https://doi.org/10.1126/science.1099192>, 2004.

805 UTCSR: Gravity Recovery and Climate Experiment UTCSR Level-2 processing
806 standards document, Issue5.0, [http://icgem.gfz-](http://icgem.gfz-potsdam.de/GRACE_CSR_L2_Processing_Standards_Document_for_RL06.pdf)
807 [potsdam.de/GRACE_CSR_L2_Processing_Standards_Document_for_RL06.pdf](http://icgem.gfz-potsdam.de/GRACE_CSR_L2_Processing_Standards_Document_for_RL06.pdf) (last
808 access: 6 November 2023), 2018.

809 Vignudelli, S., Snaith, H. M., Lyard, F., Cipollini, P., Venuti, F., Birol, F., Bouffard, J.,
810 and Roblou, L.: Satellite radar altimetry from open ocean to coasts: challenges and
811 perspectives, *Asia-Pacific Remote Sensing Symposium*, Goa, India, 64060L,
812 <https://doi.org/10.1117/12.694024>, 2006.

813 Wahr, J., Molenaar, M., and Bryan, F.: Time variability of the Earth’s gravity field:
814 Hydrological and oceanic effects and their possible detection using GRACE, *J.*
815 *Geophys. Res.*, 103, 30205–30229, <https://doi.org/10.1029/98JB02844>, 1998.

816 Wahr, J., Swenson, S., Zlotnicki, V., and Velicogna, I.: Time-variable gravity from
817 GRACE: First results: TIME-VARIABLE GRAVITY FROM GRACE, *Geophys. Res.*
818 *Lett.*, 31, n/a-n/a, <https://doi.org/10.1029/2004GL019779>, 2004.

819 Wang, Y.-L. and Wu, C.-R.: Enhanced Warming and Intensification of the Kuroshio
820 Extension, 1999–2013, *Remote Sensing*, 11, 101, <https://doi.org/10.3390/rs11010101>,
821 2019.

822 Willis, J. K., Chambers, D. P., and Nerem, R. S.: Assessing the globally averaged sea
823 level budget on seasonal to interannual timescales, *J. Geophys. Res.*, 113, C06015,
824 <https://doi.org/10.1029/2007JC004517>, 2008.

825 Wouters, B., Bonin, J. A., Chambers, D. P., Riva, R. E. M., Sasgen, I., and Wahr, J.:
826 GRACE, time-varying gravity, Earth system dynamics and climate change, Rep. Prog.
827 Phys., 77, 116801, <https://doi.org/10.1088/0034-4885/77/11/116801>, 2014.

828 Yang, Y., Feng, W., Zhong, M., Mu, D., and Yao, Y.: Basin-Scale Sea Level Budget
829 from Satellite Altimetry, Satellite Gravimetry, and Argo Data over 2005 to 2019,
830 Remote Sensing, 14, 4637, <https://doi.org/10.3390/rs14184637>, 2022.

831 Yuan, J., Guo, J., Liu, X., Zhu, C., Niu, Y., Li, Z., Ji, B., and Ouyang, Y.: Mean sea
832 surface model over China seas and its adjacent ocean established with the 19-year
833 moving average method from multi-satellite altimeter data, Continental Shelf
834 Research, 192, 104009, <https://doi.org/10.1016/j.csr.2019.104009>, 2020a.

835 Yuan, J., Guo, J., Niu, Y., Zhu, C., and Li, Z.: Mean Sea Surface Model over the Sea
836 of Japan Determined from Multi-Satellite Altimeter Data and Tide Gauge Records,
837 Remote Sensing, 12, 4168, <https://doi.org/10.3390/rs12244168>, 2020b.

838 Yuan, J., Guo, J., Zhu, C., Hwang, C., Yu, D., Sun, M., and Mu, D.: High-resolution
839 sea level change around China seas revealed through multi-satellite altimeter data,
840 International Journal of Applied Earth Observation and Geoinformation, 102, 102433,
841 <https://doi.org/10.1016/j.jag.2021.102433>, 2021.

842 Yuan, J., Guo, J., Zhu, C., Li, Z., Liu, X., and Gao, J.: SDUST2020 MSS: a global 1'
843 × 1' mean sea surface model determined from multi-satellite altimetry data, Earth Syst.
844 Sci. Data, 15, 155–169, <https://doi.org/10.5194/essd-15-155-2023>, 2023.

845 Zhang, S., Abulaitijiang, A., Andersen, O. B., Sandwell, D. T., and Beale, J. R.:
846 Comparison and evaluation of high-resolution marine gravity recovery via sea surface
847 heights or sea surface slopes, J Geod, 95, 66, [https://doi.org/10.1007/s00190-021-](https://doi.org/10.1007/s00190-021-01506-8)
848 01506-8, 2021.

849 Zhu, C., Guo, J., Yuan, J., Li, Z., Liu, X., and Gao, J.: SDUST2021GRA: global
850 marine gravity anomaly model recovered from Ka-band and Ku-band satellite
851 altimeter data, Earth Syst. Sci. Data, 14, 4589–4606, [https://doi.org/10.5194/essd-14-](https://doi.org/10.5194/essd-14-4589-2022)
852 4589-2022, 2022.

853 Zhu, F., Liu, X., Li, Z., Yuan, J., Guo, J., and Sun, H.: High spatial resolution marine
854 gravity trend determined from multisatellite altimeter data over Bay of Bengal,
855 Geophysical Journal International, 235, 2257–2267,
856 <https://doi.org/10.1093/gji/ggad368>, 2023.

857 Zhu, F., Guo, J., Zhang, H., Huang, L., Sun, H., and Liu, X.: SDUST2020MGCR: a
858 global marine gravity change rate model determined from multi-satellite altimeter
859 data, Zenodo [data set], <https://doi.org/10.5281/zenodo.10701641>, 2024.

860
861